Fuel 286 (2021) 119299

Contents lists available at ScienceDirect

Fuel

journal homepage: www.elsevier.com/locate/fuel

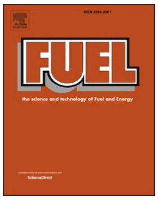

Full Length Article

CO_2-regulated octane flow in calcite nanopores from molecular perspectives

Wei Zhang [a,b,c], Qihong Feng [a,b,*], Sen Wang [a,b], Xiangdong Xing [a,b], Zhehui Jin [c,*]

[a] Key Laboratory of Unconventional Oil & Gas Development (China University of Petroleum (East China)), Ministry of Education, Qingdao 266580, PR China
[b] School of Petroleum Engineering, China University of Petroleum (East China), Qingdao 266580, PR China
[c] School of Mining and Petroleum Engineering, Department of Civil and Environmental Engineering, University of Alberta, Edmonton, AB T6G 1H9, Canada

ARTICLE INFO

Keywords:
Shale/tight oil
Calcite nanopore
Carbon dioxide
Molecular simulation
EOR mechanism

ABSTRACT

Enhanced hydrocarbon recovery from shale/tight reservoirs by CO_2 injection has gained extensive attentions in recent years. However, the effect of CO_2 on oil flow in shale/tight nanoporous media is still ambiguous. In this work, we used molecular dynamics simulations to study the structural and dynamic properties of CO_2 and nC_8 mixtures in calcite nanopores. We found that CO_2 is preferably adsorbed on the calcite surface, forming a thin CO_2 film. When CO_2 content is low, CO_2 displaces nC_8 molecules on the pore surface, while CO_2-nC_8 mixing does not occur in other regions. As the nC_8 molecules on the pore surface are immobile, the effect of CO_2 on nC_8 total flow rate is negligible. As CO_2 content further increases, only after the CO_2 adsorption layer on the pore surface is fully saturated, CO_2 can mix with nC_8 in other regions to dramatically reduce the effective viscosity of CO_2-nC_8 mixtures. As a result, nC_8 total flow rate drastically increases. This work provided important insights into the effect of CO_2 on oil flow in calcite nanopores in relation to the CO_2-EOR in shale/tight reservoirs.

1. Introduction

Owing to the continuous depletion of conventional oil reservoirs, the oil extraction from shale/tight reservoirs have been attracting growing attentions among scientists and engineers in recent years [1,2]. According to the Energy Information Administration (EIA), the global technically recoverable shale/tight oil accounts for approximately 345 billion barrels [3]. In spite of the enormous hydrocarbon reserves in shale/tight reservoirs, low efficiency and short production life have limited shale/tight oil recovery [4]. The omnipresent nanopores and the ultralow permeability of shale/tight reservoirs impose grand challenges during oil exploitation processes [5,6]. CO_2 injection is one of the most commonly deployed techniques for enhanced oil recovery (EOR) in conventional reservoirs [7]. Recent field practices also proved its efficacy in shale/tight reservoirs [8,9]. In addition, CO_2 injection into shale/tight reservoirs is one of the potential means to alleviate carbon emissions through geological CO_2 sequestration (CCS) [10,11]. During the CO_2-EOR process, the effect of CO_2 on oil flow in shale/tight nanoporous media plays a crucial role in the determination of production rate and ultimate oil recovery.

Viscosity reduction [12,13], volume expansion [14,15], extraction [16] and repressurization [17] have been proposed as the dominant CO_2-EOR mechanisms in the conventional reservoirs in previous experimental and theoretical studies. On the other hand, many experimental studies [18–21] examined the CO_2-EOR in shale/tight core samples and reported up to 80% oil recovery rate by CO_2 huff-and-puff. In addition, reservoir simulations [22–28] on CO_2 flooding and huff-and-puff also predicted a greatly improved EOR efficiency. Experimental studies hypothesized that oil swelling [29], viscosity reduction [29,30] and molecular diffusion [19] are responsible for the enhanced oil recovery in the unconventional reservoirs, while molecular diffusion [26,31,32] and extraction [33] were proposed in most numerical simulation works. Recent microfluidic experiments [34,35] also elucidated the mechanisms of light-component extraction and volume expansion due to CO_2 injection, and the efficiency of CO_2 huff-and-puff depends on the solubility and miscibility of injected CO_2 with oil. However, the nano-confinement effect in shale/tight media may lead to different CO_2-EOR mechanisms than those proposed in the conventional reservoirs, which are far from being understood from experiments and numerical simulations.

Molecular simulations have been widely used to investigate structural [36–39] and dynamic properties [40–42] of geofluids in shale/tight reservoirs. Tuan *et al.* [43] reported a supercritical CO_2-induced wettability alteration in kerogen nanopores by forming a thin CO_2 film

---

* Corresponding authors.
E-mail addresses: fengqihong.upc@gmail.com (Q. Feng), zhehui2@ualberta.ca (Z. Jin).

https://doi.org/10.1016/j.fuel.2020.119299
Received 4 July 2020; Received in revised form 17 September 2020; Accepted 20 September 2020

Table 1
Force field parameters of nC_8, CO_2 and calcite [54,57,58].

Species	Type	Molecular Weight, g/mol	$\varepsilon/k_B, K$	σ, Å	q, e
nC_8	Methyl $-CH_3$	15.035	88.063	3.905	0
	Methylene $-CH_2$	14.027	59.38	3.905	0
CO_2	C	12.011	28.129	2.757	0.6512
	O	15.999	80.507	3.033	−0.3256
Calcite	Ca	40.078	240.58	2.370	1.668
	C_M	12.011	44.38	3.823	0.999
	O_M	15.999	70.0	3.091	−0.889

ε and σ are the Lennard-Jones energy and size parameters, respectively; q is the atomic charge.

Table 2
The number of nC_8 and CO_2 molecules and the external force in each system.

Oil mass percentage, %	Number of nC_8 molecules	Number of CO_2 molecules	External force, Kcal/mol-Å
100	700	0	0.002335
92	650	150	0.002315
83	600	300	0.002294
81	580	350	0.002299
76	550	450	0.002275
71	520	530	0.002275
68	500	600	0.002255
50	380	950	0.00222

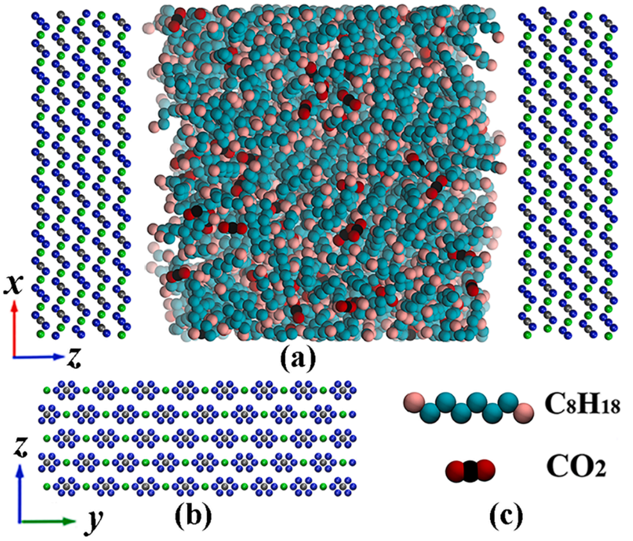

Fig. 1. (a) Schematic representation of the initial configurations of nC_8 and CO_2 molecules in calcite nanopores. (b) Side view of the calcite sheet. (c) Molecular structures of nC_8 and CO_2. Color scheme: cyan, methyl group ($-CH_3$); pink, methylene group ($-CH_2$); dark red, O in CO_2; black, C in CO_2; green, Ca; blue, O in calcite; gray, C in calcite. (For interpretation of the references to color in this figure legend, the reader is referred to the web version of this article.)

on the surface, which significantly enhances water flow. Santos *et al.* [44] found that n-alkane in calcite nanopores can be displaced by CO_2, which illustrates the applicability of CO_2 injection into shale/tight formations to enhance oil recovery. Recently, Zhu *et al.* [45] reported that CO_2 can displace the adsorbed nC_{10} and nC_{17} on calcite surface forming a thin CO_2 film. They concluded that CO_2 injection can mitigate the hydrocarbon sieving effects to increase the oil flow rate and the surface property alteration plays an essential role on CO_2-EOR. Fang *et al.* [46] studied the miscibility and displacement of CO_2/C_{10} in various nanopores. They revealed that the stability of displacement front is important to oil migration. Although these studies enriched the understanding about CO_2-EOR in various shale/tight nanopores, the fundamental understanding about the effect of CO_2 on oil flow in shale/tight nanopores from molecular perspectives still remains unclear.

In this work, we use molecular dynamics (MD) simulations to study the effect of CO_2 on oil flow in calcite nanopores. Calcite is one of the major constituents in shale/tight reservoirs, which not only provides hydrocarbon storage space, but also affords the potential sites for geological CO_2 sequestration [42,44]. We use nC_8 to represent oil in this work. The simulations are conducted at a typical shale/tight reservoir condition (343 K and 30 MPa) [47,48]. Shale/tight reservoirs contain a large proportion of mesopores [6,37,49] with a slit-like geometry according to scanning electron microscope (SEM) images [50–52]. Thus, 5-nm calcite slit nanopores containing CO_2-nC_8 mixtures with varying compositions are constructed. We explicitly study the effect of CO_2 on structural and flow behaviors of nC_8 in calcite nanopores to provide important insights into CO_2-EOR in shale/tight reservoirs.

2. Simulation method

2.1. Molecular model

In this work, the calcite surface is constructed based on the $\{10\overline{1}4\}$ plane orthogonal to the z-direction, which is the most stable surface [53]. The thickness of each calcite sheet is 12.12 Å in the z-direction, with the x-y dimension as 74.85 Å × 48.58 Å. Two calcite sheets are used to form a slit-like calcite nanopore with a pore size H defined as the separation distance in the z-direction between the O atoms in the innermost planes. The force field proposed by Xiao *et al.* [54] is adopted to describe calcite, which has been used to study the calcite-alkane [42,44] and calcite-biomolecule systems [55]. nC_8 is used to represent the shale/tight oil [56], which is described by the OPLS-UA model [57]. CO_2 molecules are modeled by EPM2 force field [58], in which CO_2 molecules are kept rigid with a fixed C-O bond length of 1.149 Å and a fixed O-C-O bond angle of 180°. The force field parameters are summarized in Table 1.

Initially, nC_8 and CO_2 molecules are randomly placed in calcite nanopores as shown in Fig. 1**(a)**. The number of nC_8 and CO_2 molecules in the system depends on their compositions, which are determined by H, pressure and oil mass percentage (OMP) of CO_2-nC_8 mixtures. The number of nC_8 and CO_2 molecules with varying compositions is presented in Table 2. A two-dimensional periodic boundary condition is applied only in the x- and y-directions. A 20-nm vacuum slab is added in the z-direction to minimize the long-range electrostatic interaction [59]. Lorentz-Berthelot mixing rule [60] is adopted to calculate the interactions between different molecules. The cutoff distance of the non-bonded interactions is set as 12 Å [59]. We calculate the long-range electrostatic interactions by the particle–particle–particle-mesh (PPPM) method [61].

2.2. Simulation details

Molecular dynamics simulations are conducted by large-scale atomic massively parallel simulator (LAMMPS) package [62]. The system temperature is set as 343 K, which is controlled by the Nosé-Hoover thermostat [63] with a relaxation time of 0.1 ps. In this work, we use the normal pressure to the calcite surface in the z-direction P_z to dictate the pore pressure, which is set as 30 MPa. To control P_z, we fix the lower calcite sheet, while applying a uniform external force to each atom in the upper one as a piston in the z-direction. Both sheets are kept as rigid bodies. The external force f can be obtained by P_z and the number of atoms in the upper calcite sheet N,

$$f = \frac{p_z \times A}{N} \tag{1}$$

where A is the area of the upper calcite sheet in the x-y plane. After a 3-ns pressure control, the resulting H is 5 ± 0.15 nm for all OMPs. Then,

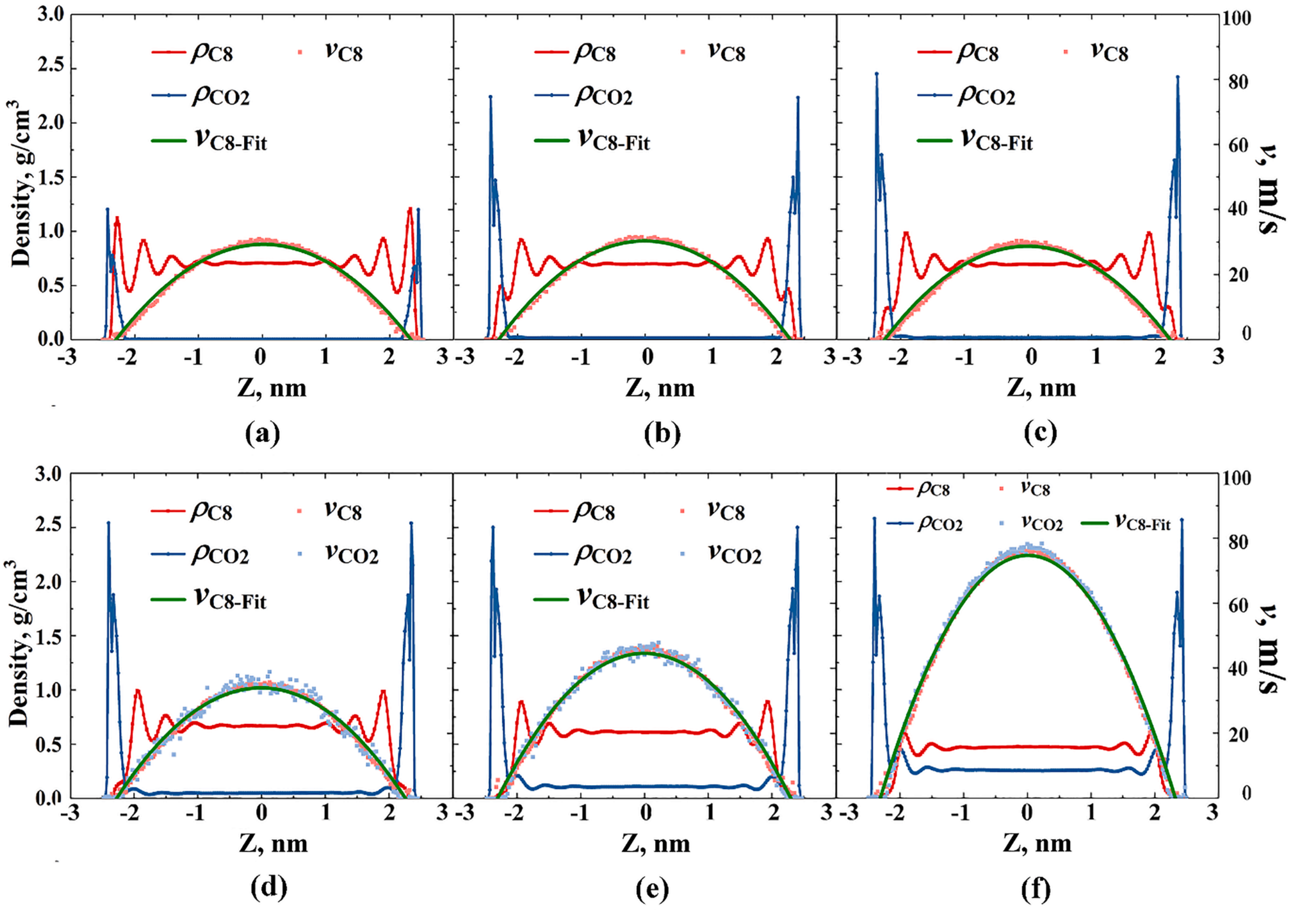

Fig. 2. Density and velocity profiles of CO_2 and nC_8 in calcite nanopores for (a) OMP = 92%; (b) OMP = 83%; (c) OMP = 81%; (d) OMP = 76%; (e) OMP = 68%; (f) OMP = 50%. The blue and red solid lines represent the CO_2 and nC_8 density distributions, respectively; the blue and red solid dots are the CO_2 and nC_8 velocity distributions, respectively; the green solid lines represent the parabolic fitting of nC_8 velocity profile. When OMP $\geq$ 81%, the number of CO_2 molecules in the middle of the pore is negligible, while the CO_2 adsorption layer is immobile. Thus, we present CO_2 velocity profiles in (d), (e), and (f) only. (For interpretation of the references to color in this figure legend, the reader is referred to the web version of this article.)

both calcite sheets are fixed and a 3-ns simulation is conducted in the *NVT* ensemble to reach the equilibrium. The atomic trajectories of another 3-ns simulation are collected to analyze equilibrium properties.

Finally, a pressure-driven flow along the *x*-direction is conducted by using external field nonequilibrium molecular dynamics (EF-NEMD) simulation [64] by applying equal external force to each atom in the

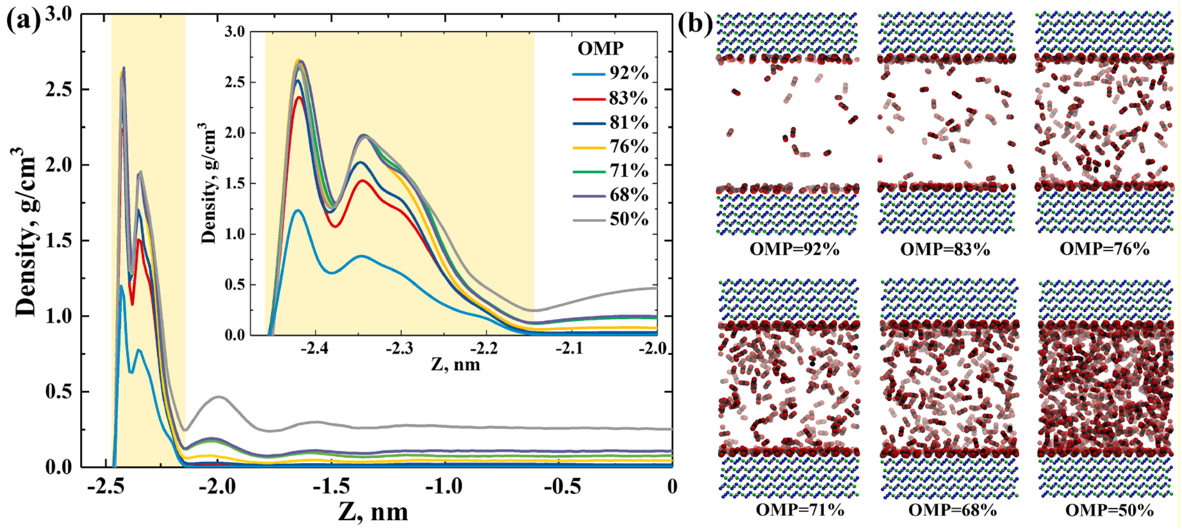

Fig. 3. (a) CO_2 density distributions for different OMP cases. (b) CO_2 molecular configurations in calcite nanopores for different OMP cases. For clarity, nC_8 molecules are omitted.

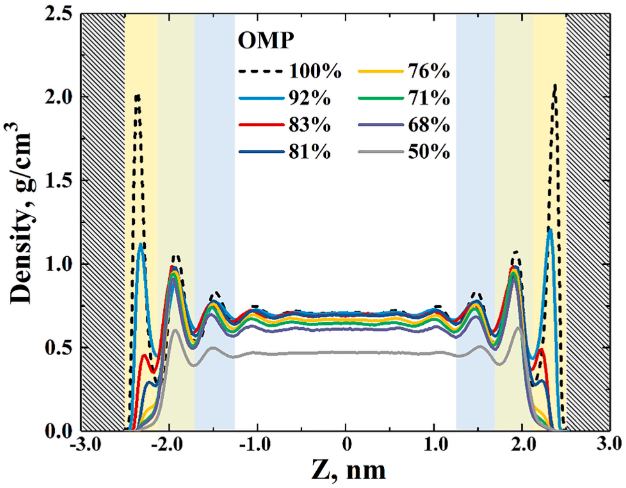

Fig. 4. nC8 density distributions for different OMP cases. The gray regions represent substrates, light yellow regions represent AL1, light green regions represent AL2, light blue region represents AL3, and white region represent BL. (For interpretation of the references to color in this figure legend, the reader is referred to the web version of this article.)

CO_2-nC_8 mixtures in calcite nanopores to investigate nC_8 and CO_2 flow behaviors. The thermostat in the EF-NEMD simulations is only coupled with molecular velocities in the y-direction. We apply the same pressure gradient dp/dL_x for different OMP cases, which is given as,

$$\frac{dp}{dL_x} = \frac{f_{ex} \times N_{fluid}}{L_y \times L_z} \quad (2)$$

where f_{ex} is the external force applied on each atom of fluids, N_{fluid} is the total number of fluid atoms, L_x, L_y, and L_z are the dimensional length in the x-, y-, z-directions. f_{ex} in different OMP cases are listed in Table 2, with a constant pressure gradient as 5 MPa/nm. Such high-pressure gradient is employed to minimize the thermal fluctuation and reduce the computational cost [65]. 15-ns EF-NEMD simulations are conducted, in which the last 10-ns trajectories are used for sampling dynamic properties.

3. Results and discussion

In this section, we first present the density distributions of CO_2 and nC_8 in calcite nanopores of varying OMPs. Then, we discuss their flow behaviors in calcite nanopores and explicitly study the effect of CO_2 on oil flow. We note that $z = 0$ represents the middle of the pores throughout this section.

3.1. Mass density profiles

In Fig. 2, we present the density profiles of CO_2 and nC_8 in calcite nanopores of varying OMPs. We note that density profiles from the equilibrium MD and EF-NEMD simulations are literally the same [65]. It reveals that CO_2 is preferably adsorbed on the pore surface, showing a stronger affinity to the calcite surface than nC_8. Such phenomenon is also observed in Zhu *et al.* [45]. It is probably because CO_2 has a strong quadruple moment [66], while nC_8 only has a Van der Waals type interaction with the calcite substrate. The CO_2 adsorption peak value increases as OMP decreases until reaching ~2.5 g/cm^3, as shown in Fig. 2**(c)**. Before the CO_2 adsorption layer is completely formed on the pore surface, the CO_2 density in the middle of the pore is approximately zero, while the nC_8 density in the middle of the pore is close to 0.70 g/cm^3, consistent with its bulk density at the given temperature and pressure [68]. The variations in CO_2 density distributions as OMP varies are presented in Fig. 3**(a)**. Although there are two peaks near the pore surface, CO_2 has a monolayer adsorption, while the O atoms in CO_2 molecules are preferentially attracted by Ca atoms in calcite, leading to a ~60° orientation angle between CO_2 atom and the pore surface. This phenomenon is confirmed by CO_2 molecular configurations depicted in Fig. 3**(b)** and CO_2 orientation parameters (see **Supporting Information Figures S3–S5**). The peak value of CO_2 adsorption layer increases as OMP decreases until OMP = 81%. As OMP further decreases, the CO_2 adsorption layer is saturated, while its density in the middle of the pore increases. It indicates that when CO_2 content is small, CO_2 molecules are preferably adsorbed on the calcite surface; only after the CO_2 adsorption layer is fully saturated forming a thin CO_2 film, CO_2 can mix with nC_8 in the middle of the pores. The thickness of a fully formed CO_2 film which is defined as the distance from the pore surface to the second saddle point in CO_2 density profiles (note that the first saddle point is due to CO_2 orientation) as shown in Fig. 3**(a)**, is approximately 3.25 Å and independent of OMP.

To better understand the effect of CO_2 on the structural properties of nC_8 in calcite nanopores, we present nC_8 density distributions for varying OMPs in Fig. 4. It shows that without CO_2, nC_8 has a layering structure near the pore surface with the peak value of its first adsorption layer around 2.1 g/cm^3, while its density in the middle of the pores approaches the bulk. As OMP decreases, nC_8 molecules are continuously displaced from the pore surface, while changes in other adsorption layers and bulk regions are negligible until OMP decreases to 81%. When OMP < 81%, the first adsorption layer of nC_8 is completely displaced by CO_2 and nC_8 densities in other regions start decreasing. The changes in nC_8 density distributions with OMP indicate that CO_2 displaces the first adsorption layer of nC_8 firstly, and then mix with nC_8 in other regions.

3.2. Velocity profiles and flow behaviors

The velocity profiles of nC_8 and CO_2 for different OMP cases under a pressure gradient of 5 MPa/nm are presented in Fig. 2. We note that when OMP ≥ 81% (Fig. 2**(a-c)**), the number of CO_2 molecules in the middle of the pores is negligible, while CO_2 molecules on the pore surface is immobile. Thus, we only present the CO_2 velocity profiles when OMP < 81%. It shows that the velocity profiles of nC_8 and CO_2 are both parabolic-shaped. When OMP ≥ 81%, as nC_8 molecules on the pore surface are immobile and CO_2 does not mix with nC_8 in the middle of the pores, the effect of CO_2 on nC_8 velocity distributions is negligible. However, when OMP < 81%, both CO_2 and nC_8 velocity distributions increase dramatically as OMP decreases as shown in Fig. 2**(d-f)**. The enhanced nC_8 velocity in the flow direction can be attributed to the viscosity reduction due to CO_2 mixing in the middle of the pores. Due to the presence of CO_2 film, the negative slip velocity that occurs in pure alkane flow [42] is not observed. On the other hand, it has been reported that fluid flow and velocity profiles can be also dependent on the relative magnitude of pressure gradients and resistance [67]. We fit the nC_8 velocity profiles with a 2nd-order polynomial equation as $v(z) = az^2 + c$. As shown in Fig. 2, the fitted curves match perfectly with nC_8 velocity profiles obtained from EF-NEMD simulations. Therefore, nC_8 velocity profiles can be described by the classical Poiseuille equation,

$$v(z) = -\frac{\nabla p}{2\eta}\left(z^2 - \frac{H^2}{4}\right) \quad (3)$$

where η is the fluid viscosity.

To better understand the effect of CO_2 on nC_8 flow, we separate the calcite nanopore space into three adsorption-layer regions (AL1, AL2, and AL3) and one bulk-like region (BL) as shown in Fig. 4, which are distinguished according to nC_8 density profiles. We compute the local flow rate Q_k and local reduced velocity $v_{R,k}$ in each region,

$$Q_k = \int_{z_{i,k}}^{z_{j,k}} \rho_n(z)v(z)dz \ (k = \text{AL1, AL2, AL3, BL}) \quad (4)$$

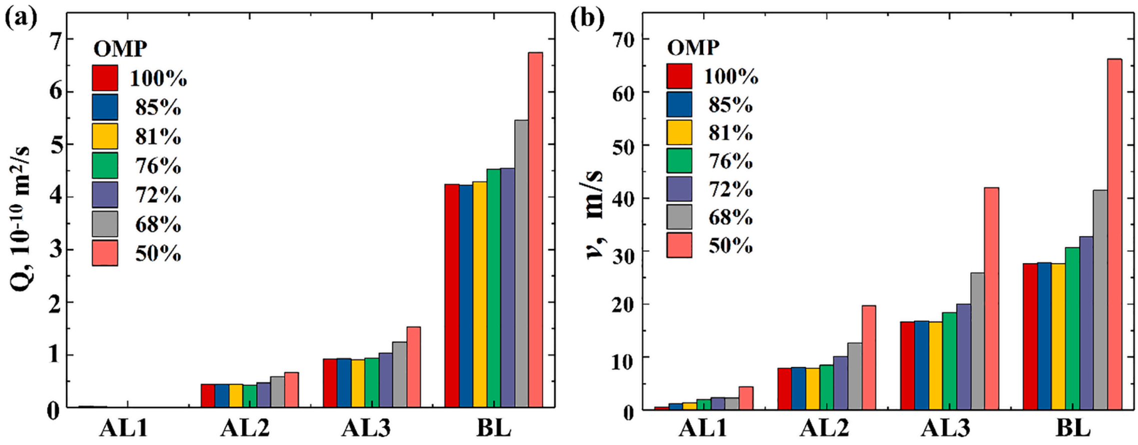

Fig. 5. (a) Q_k; (b) $v_{R,k}$ in AL1, AL2, AL3, and BL for various OMPs.

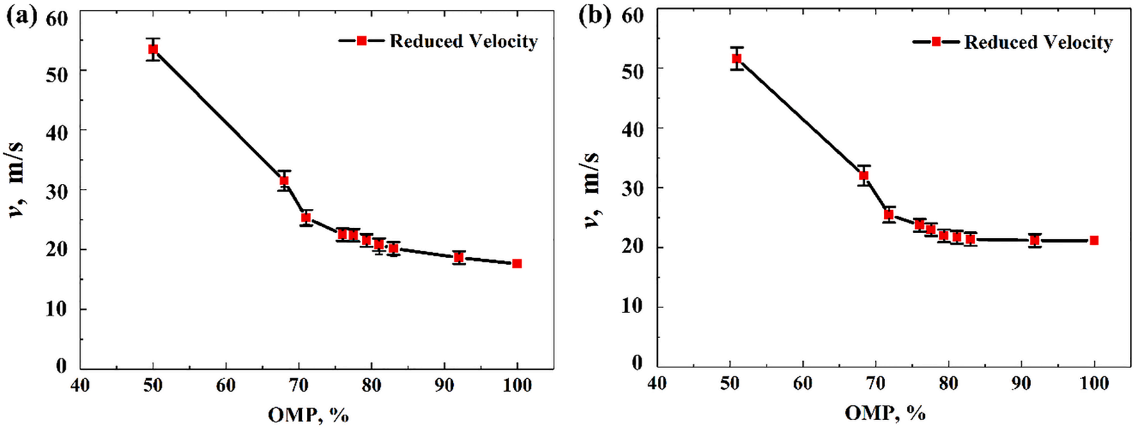

Fig. 6. Overall nC_8 reduced velocity (a) with AL1; (b) without AL1.

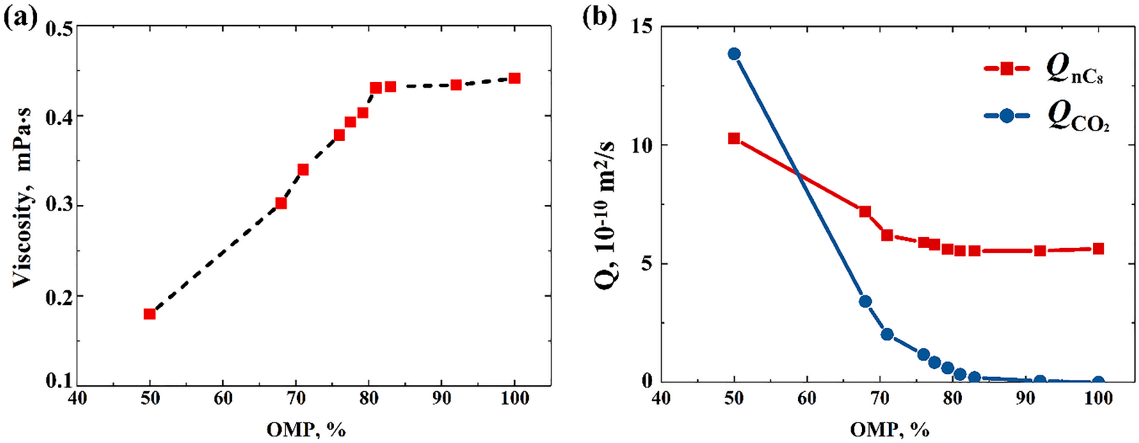

Fig. 7. (a) η_{eff}; (b) overall nC_8 and CO_2 flow rates for various OMP cases.

$$v_{R,k} = \frac{\int_{z_{i,k}}^{z_{j,k}} \rho_n(z) v(z) dz}{\int_{z_{i,k}}^{z_{j,k}} \rho_n(z) dz} \quad (k = \text{AL1, AL2, AL3, BL}) \qquad (5)$$

where z_i and z_j are the lower and upper limits in z-direction of each region, ρ_n represents the number density of nC_8. Q_k and $v_{R,k}$ in each region for various OMPs are shown in Fig. 5. It shows that nC_8 flow in AL1 is negligible. The fluids closer to the calcite pore surface have a smaller $v_{R,k}$. When OMP $\geq$ 81%, Q_k and $v_{R,k}$ in AL2, AL3, and BL remain largely unchanged. It is because CO_2 molecules are preferably adsorbed on the pore surface, while they do not mix with nC_8 in these regions. On the other hand, when OMP $<$ 81%, as the CO_2 content increases, Q_k and $v_{R,k}$ in AL2, AL3, and BL increase, thanks to the CO_2-nC_8 mixing in these regions. In Fig. 6, we present the overall nC_8 reduced velocities for various OMPs with/without considering AL1. With considering AL1, the overall nC_8 reduced velocities monotonically increase as OMP decreases. For 100% $\geq$ OMP $\geq$ 81%, as OMP decreases, the fraction of nC_8 in AL1 continuously decreases; for OMP $<$ 81%, CO_2-nC_8 mixing occurs

Table 3
η_{eff} of CO_2-nC_8 binary mixtures for various OMP cases.

Oil mass percentage, %	Fitted parameter a, $10^{18}m^{-1}s^{-1}$	Effective viscosity, mPa·s
100	−5.6937	0.439084
92	−5.7637	0.43375
83	−5.7858	0.43209
81	−5.8057	0.43061
79.4	−6.20154	0.40312
77.5	−6.36172	0.3929
76	−6.6096	0.37824
71	−7.2525	0.344708
68	−8.3604	0.29903
50	−13.9245	0.17954

in AL2, AL3, and BL to lower viscosity. However, without considering AL1, the overall nC_8 reduced velocity remains constant for 100% $\geq$ OMP $\geq$ 81%.

The effective viscosity can be obtained from the parabolic fitting to nC_8 velocity profiles. According to Eq. (3), the effective viscosity η_{eff} can be given as

$$\eta_{eff} = -\nabla p / 2a \tag{6}$$

We present η_{eff} for various OMP cases in Fig. 7**(a)**. The fitted parameters and η_{eff} are also listed in Table 3. For 100% $\geq$ OMP $\geq$ 81%, η_{eff} is rather constant and agrees well with the bulk nC_8 viscosity (0.43234 mPa·s) at the given temperature and pressure from NIST Chemistry Webbook [68], as CO_2-nC_8 does not occur in AL2, AL3, and BL where nC_8 can flow. For OMP < 81%, η_{eff} drops dramatically as OMP decreases. In Fig. 7**(b)**, we also present the overall nC_8 and CO_2 flow rates. It shows that both nC_8 and CO_2 flow rates remain constant for 100% $\geq$ OMP $\geq$ 81%. On the other hand, as η_{eff} reduces due to the CO_2-nC_8 mixing in AL2, AL3, and BL, both flow rates dramatically increase as OMP decreases for OMP < 81%.

4. Conclusion

In this work, we studied the structural and dynamic properties of CO_2-nC_8 binary mixtures in 5-nm calcite nanopores at 343 K and 30 MPa by MD simulations. We find that CO_2 is preferably adsorbed on the calcite pore surface with a monolayer adsorption. While CO_2 can displace nC_8 molecules in the first adsorption layer, CO_2-nC_8 mixing in AL2, AL3, and BL can only occur OMP drops below the critical OMP. As only nC_8 in these regions can flow along the flow direction, the enhancement of nC_8 flow due to the addition of CO_2 is negligible when OMP is less than the critical OMP. Both CO_2 and nC_8 velocity distributions are parabolic shaped under a pressure gradient, suggesting the feasibility of the classical continuous hydrodynamics equation. There exists a critical OMP (81% in this work) beyond which CO_2 can only displace adsorbed nC_8 on the pore surface, while having a negligible impact on oil flow; below which CO_2 can mix with nC_8 and oil viscosity is greatly reduced. We should note that the critical OMP is strongly dependent on pore size, while system temperature and pressure may also play a role.

Our study advances the understanding of CO_2-nC_8 structural and dynamic properties in calcite nanopores and provides some important insights into the CO_2-EOR mechanisms in shale/tight reservoirs nanopores, which can serve as a theoretical foundation for the development of numerical simulations on CO_2-EOR from the unconventional reservoirs. On the other hand, this work focuses on one particular pore size case at given temperature and pressure. However, calcite in shale/tight formations has pore size distributions ranging widely from nanometers to micrometers [69,70]. The effect of pore size on CO_2-EOR mechanism should be investigated in the future works.

CRediT authorship contribution statement

Wei Zhang: Methodology, Software, Validation, Formal analysis, Investigation, Writing - original draft, Writing - review & editing, Visualization. **Qihong Feng:** Conceptualization, Formal analysis, Investigation, Resources, Writing - review & editing, Supervision, Funding acquisition. **Sen Wang:** Conceptualization, Formal analysis, Investigation, Resources, Writing - review & editing, Supervision. **Xiangdong Xing:** Formal analysis, Investigation, Resources, Writing - review & editing. **Zhehui Jin:** Conceptualization, Formal analysis, Investigation, Resources, Writing - review & editing, Supervision, Funding acquisition.

Declaration of Competing Interest

The authors declare that they have no known competing financial interests or personal relationships that could have appeared to influence the work reported in this paper.

Acknowledgements

The authors acknowledge China Scholarship Council (CSC) for financial support provided to W. Zhang. This research was enabled in part by support provided by Westgrid (www.westgrid.ca) and Compute Canada (www.computecanada.ca). This study was supported by the National Natural Science Foundation of China (U1762213, 51704312), the National Science and Technology Major Project (2017ZX05071), Program for Changjiang Scholars and Innovative Research Team in University (IRT1294), the Applied Fundamental Research Project of Qingdao (Grant No. 19-6-2-21-cg); the Fundamental Research Funds for the Central Universities (18CX07006A), and Discovery Grant from Natural Sciences and Engineering Research Council of Canada (NSERC RGPIN-2017-05080).

Appendix A. Supplementary data

Supplementary data to this article can be found online at https://doi.org/10.1016/j.fuel.2020.119299.

References

[1] Salama A, Amin MFE, Kumar K, Sun S. Flow and transport in tight and shale formations: a review. Geofluids 2017;2017:4251209.
[2] Boak J, Kleinberg R. Shale Gas, Tight Oil, Shale Oil and Hydraulic Fracturing Future Energy. Elsevier; 2020. p. 67–95.
[3] Administration. EI. Technically Recoverable Shale Oil and Shale Gas Resources; Available from: https://www.eia.gov/todayinenergy/detail.php?id=14431; 2014.
[4] Jia B, Tsau J-S, Barati R. A review of the current progress of CO2 injection EOR and carbon storage in shale oil reservoirs. Fuel 2019;236:404–27.
[5] Wu T, Zhao J, Zhang W, Zhang D. Nanopore structure and nanomechanical properties of organic-rich terrestrial shale: an insight into technical issues for hydrocarbon production. Nano Energy 2020;69:104426.
[6] Ross DJK, Marc BR. The importance of shale composition and pore structure upon gas storage potential of shale gas reservoirs. Mar Pet Geol 2009;26(6):916–27.
[7] Alfarge D, Wei M, Bai B. Comparative analysis between CO2-EOR mechanisms in conventional reservoirs versus shale and tight reservoirs. Developments in Petroleum Science. Elsevier; 2020. p. 45–63.
[8] Song C, Yang DT. Optimization of CO2 Flooding Schemes for Unlocking Resources from Tight Oil Formations. In: SPE Canadian Unconventional Resources Conference. Calgary, Alberta, Canada: Society of Petroleum Engineers; 2012, p. 17.
[9] Merey S, Sinayuc C. Analysis of carbon dioxide sequestration in shale gas reservoirs by using experimental adsorption data and adsorption models. J Nat Gas Sci Eng 2016;36:1087–105.
[10] Pranesh V. Subsurface CO2 storage estimation in Bakken tight oil and Eagle Ford shale gas condensate reservoirs by retention mechanism. Fuel 2018;215:580–91.
[11] Bui M, Adjiman CS, Bardow A, Anthony EJ, Boston A, Brown S, et al. Carbon capture and storage (CCS): the way forward. Energy Environ Sci 2018;11(5):1062–176.
[12] Holm LW, Josendal VA. Mechanisms of Oil Displacement By Carbon Dioxide. SPE-4736-PA 1974;26(12):1427–38.
[13] Li H, Zheng S, Yang D. Enhanced swelling effect and viscosity reduction of solvent(s)/CO2/heavy-oil systems. SPE J 2013;18(04):695–707.

[14] Liu B, Shi J, Sun B, Shen Y, Zhang J, Chen X, et al. Molecular dynamics simulation on volume swelling of CO2–alkane system. Fuel 2015;143:194–201.

[15] Yang Z, Li M, Peng B, Lin M, Dong Z. Volume expansion of CO2+ oil at near critical and supercritical conditions of CO2. Fuel 2013;112:283–8.

[16] Zhou X, Yuan Q, Peng X, Zeng F, Zhang L. A critical review of the CO2 huff 'n' puff process for enhanced heavy oil recovery. Fuel 2018;215:813–24.

[17] Holtz MH, Nance PK, Finley RJ. Reduction of greenhouse gas emissions through CO2 EOR in Texas. Environ Geosci 2001;8(3):187–99.

[18] Jin L, Hawthorne S, Sorensen J, Pekot L, Kurz B, Smith S, et al. Advancing CO2 enhanced oil recovery and storage in unconventional oil play—experimental studies on Bakken shales. Appl Energy 2017;208:171–83.

[19] Jin L, Sorensen JA, Hawthorne SB, Smith SA, Bosshart NW, Burton-Kelly ME, et al. Improving oil transportability using CO2 in the Bakken system–a laboratory investigation. SPE International Conference and Exhibition on Formation Damage Control. Society of Petroleum Engineers; 2016.

[20] Alharthy N, Teklu TW, Kazemi H, Graves RM, Hawthorne SB, Braunberger J, et al. Enhanced oil recovery in liquid-rich shale reservoirs: laboratory to field. SPE-168880-PA 2018;21(01):137–59.

[21] Tovar FD, Eide O, Graue A, Schechter DS. Experimental Investigation of Enhanced Recovery in Unconventional Liquid Reservoirs using CO2: A Look Ahead to the Future of Unconventional EOR. SPE Unconventional Resources Conference. The Woodlands, Texas, USA: Society of Petroleum Engineers; 2014:9.

[22] Sheng JJ. Increase liquid oil production by huff-n-puff of produced gas in shale gas condensate reservoirs. J Unconvent Oil Gas Resources 2015;11:19–26.

[23] Sheng JJ. Critical review of field EOR projects in shale and tight reservoirs. J Petrol Sci Eng 2017;159:654–65.

[24] Alfarge D, Wei M, Bai B. Factors affecting CO2-EOR in shale-oil reservoirs: numerical simulation study and pilot tests. Energy Fuels 2017;31(8):8462–80.

[25] Zuloaga-Molero P, Yu W, Xu Y, Sepehrnoori K, Li B. Simulation study of CO2-EOR in tight oil reservoirs with complex fracture geometries. Sci Rep 2016;6(1):33445.

[26] Yu W, Lashgari HR, Wu K, Sepehrnoori K. CO2 injection for enhanced oil recovery in Bakken tight oil reservoirs. Fuel 2015;159:354–63.

[27] Sun R, Yu W, Xu F, Pu H, Miao J. Compositional simulation of CO2 Huff-n-Puff process in Middle Bakken tight oil reservoirs with hydraulic fractures. Fuel 2019; 236:1446–57.

[28] Chen C, Gu M. Investigation of cyclic CO2 huff-and-puff recovery in shale oil reservoirs using reservoir simulation and sensitivity analysis. Fuel 2017;188: 102–11.

[29] Li L, Wang C, Li D, Fu J, Su Y, Lv Y. Experimental investigation of shale oil recovery from Qianjiang core samples by the CO2 huff-n-puff EOR method. RSC Adv 2019;9 (49):28857–69.

[30] Pu W, Wei B, Jin F, Li Y, Jia H, Liu P, et al. Experimental investigation of CO2 huff-n-puff process for enhancing oil recovery in tight reservoirs. Chem Eng Res Des 2016;111:269–76.

[31] Wan T, Meng X, Sheng JJ, Watson M. Compositional Modeling of EOR Process in Stimulated Shale Oil Reservoirs by Cyclic Gas Injection. In: SPE Improved Oil Recovery Symposium. Tulsa, Oklahoma, USA: Society of Petroleum Engineers; 2014:19.

[32] Alfarge D, Wei M, Bai B, Almansour A. Effect of Molecular-Diffusion Mechanisim on CO_2 Huff-n-Puff Process in Shale-Oil Reservoirs. In: SPE Kingdom of Saudi Arabia Annual Technical Symposium and Exhibition. Dammam, Saudi Arabia: Society of Petroleum Engineers; 2017. p. 17.

[33] Mohagheghian E, Hassanzadeh H, Chen Z. CO2 sequestration coupled with enhanced gas recovery in shale gas reservoirs. J CO2 Util 2019;34:646–55.

[34] Nguyen P, Carey JW, Viswanathan HS, Porter M. Effectiveness of supercritical-CO2 and N2 huff-and-puff methods of enhanced oil recovery in shale fracture networks using microfluidic experiments. Appl Energy 2018;230:160–74.

[35] Zhang K, Jia N, Li S, Liu L. Static and dynamic behavior of CO2 enhanced oil recovery in shale reservoirs: experimental nanofluidics and theoretical models with dual-scale nanopores. Appl Energy 2019;255:113752.

[36] Wang H, Qu Z, Yin Y, Bai J, Yu B. Review of molecular simulation method for gas adsorption/desorption and diffusion in shale matrix. J Therm Sci 2019;28(1):1–16.

[37] Wang S, Feng Q, Javadpour F, Hu Q, Wu K. Competitive adsorption of methane and ethane in montmorillonite nanopores of shale at supercritical conditions: a grand canonical Monte Carlo simulation study. Chem Eng J 2019;355:76–90.

[38] Zeng K, Jiang P, Lun Z, Xu R. Molecular simulation of carbon dioxide and methane adsorption in shale organic nanopores. Energy Fuels 2018;33(3):1785–96.

[39] Zhou J, Jin Z, Luo KH. Insights into recovery of multi-component shale gas by CO2 injection: a molecular perspective. Fuel 2020;267:117247.

[40] Liu B, Wang C, Zhang J, Xiao S, Zhang Z, Shen Y, et al. Displacement mechanism of oil in shale inorganic nanopores by supercritical carbon dioxide from molecular dynamics simulations. Energy Fuels 2017;31(1):738–46.

[41] Nan Y, Li W, Jin Z. Slip length of methane flow under shale reservoir conditions: effect of pore size and pressure. Fuel 2020;259:116237.

[42] Wang S, Feng Q, Javadpour F, Yang Y-B. Breakdown of fast mass transport of methane through calcite nanopores. J Phys Chem C 2016;120(26):14260–9.

[43] Ho TA, Wang Y, Ilgen A, Criscenti LJ, Tenney CM. Supercritical CO 2-induced atomistic lubrication for water flow in a rough hydrophilic nanochannel. Nanoscale 2018;10(42):19957–63.

[44] Santos MS, Franco LF, Castier M, Economou IG. Molecular dynamics simulation of n-alkanes and CO2 confined by calcite nanopores. Energy Fuels 2018;32(2): 1934–41.

[45] Zhu Z, Fang C, Qiao R, Yin X, Ozkan E. Experimental and molecular insights on mitigation of hydrocarbon sieving in niobrara shale by CO2 Huff 'n'Puff. SPE J 2020.

[46] Fang T, Zhang Y, Ding B, Yan Y, Zhang J. Static and dynamic behavior of CO2 enhanced oil recovery in nanoslits: Effects of mineral type and oil components. Int J Heat Mass Transf 2020;153:119583.

[47] Xiong Y, Winterfeld P, Wang C, Huang Z, Wu Y-S. Effect of Large Capillary Pressure on Fluid Flow and Transport in Stress-sensitive Tight Oil Reservoirs. In: SPE Annual Technical Conference and Exhibition. Houston, Texas, USA: Society of Petroleum Engineers; 2015, p. 26.

[48] Tran T, Sinurat PD, Wattenbarger BA. Production Characteristics of the Bakken Shale Oil. In: SPE Annual Technical Conference and Exhibition. Denver, Colorado, USA: Society of Petroleum Engineers; 2011. p. 14.

[49] Chen G, Lu S, Liu K, Xue Q, Xu C, Tian S, et al. Investigation of pore size effects on adsorption behavior of shale gas. Mar Pet Geol 2019;109:1–8.

[50] Afsharpoor A, Javadpour F. Liquid slip flow in a network of shale noncircular nanopores. Fuel 2016;180:580–90.

[51] Zhang S, Yan J, Hu Q, Wang J, Tian T, Chao J, et al. Integrated NMR and FE-SEM methods for pore structure characterization of Shahejie shale from the Dongying Depression, Bohai Bay Basin. Mar Pet Geol 2019;100:85–94.

[52] Wu K, Chen Z, Li X. Real gas transport through nanopores of varying cross-section type and shape in shale gas reservoirs. Chem Eng J 2015;281:813–25.

[53] Wright K, Catlow R, Catlow CRA. Minerals ASIMPP, Division NATOSA. Microscopic Properties and Processes in Minerals. Springer Netherlands; 1999.

[54] Xiao S, Edwards SA, Gräter F. A new transferable forcefield for simulating the mechanics of CaCO3 crystals. J Phys Chem C 2011;115(41):20067–75.

[55] Zhu B, Xu X, Tang R. Hydration layer structures on calcite facets and their roles in selective adsorptions of biomolecules: a molecular dynamics study. J Chem Phys 2013;139(23):234705.

[56] Zhang W, Feng Q, Wang S, Xing X. Oil diffusion in shale nanopores: insight of molecular dynamics simulation. J Mol Liq 2019;290:111183.

[57] Jorgensen WL, Maxwell DS, Tirado-Rives J. Development and testing of the OPLS all-atom force field on conformational energetics and properties of organic liquids. J Am Chem Soc 1996;118(45):11225–36.

[58] Harris JG, Yung KH. Carbon dioxide's liquid-vapor coexistence curve and critical properties as predicted by a simple molecular model. J Phys Chem 1995;99(31): 12021–4.

[59] Frenkel D, Smit B. Understanding molecular simulation: from algorithms to applications. Elsevier; 2001.

[60] Lorentz H. Ueber die Anwendung des Satzes vom Virial in der kinetischen Theorie der Gase. Ann Phys 1881;248(1):127–36.

[61] Eastwood JW, Hockney RW, Lawrence D. P3M3DP—the three-dimensional periodic particle-particle/particle-mesh program. Comput Phys Commun 1980;19 (2):215–61.

[62] Plimpton S. Fast parallel algorithms for short-range molecular dynamics. J Comput Phys 1995;117(1):1–19.

[63] Evans DJ, Holian BL. The Nose-Hoover thermostat. J Chem Phys 1985;83(8): 4069–74.

[64] Arya G, Chang H-C, Maginn EJ. A critical comparison of equilibrium, non-equilibrium and boundary-driven molecular dynamics techniques for studying transport in microporous materials. J Chem Phys 2001;115(17):8112–24.

[65] Zhan S, Su Y, Jin Z, Wang W, Li L. Effect of water film on oil flow in quartz nanopores from molecular perspectives. Fuel 2020;262:116560.

[66] Jin Z, Firoozabadi A. Methane and carbon dioxide adsorption in clay-like slit pores by Monte Carlo simulations. Fluid Phase Equilib 2013;360:456–65.

[67] Miao Q, Yuan Q, Zhao Y-P. Dissolutive flow in nanochannels: transition between plug-like and Poiseuille-like. Microfluid Nanofluid 2018;22(12):141.

[68] Lemmon E, McLinden M, Friend D, Linstrom P, Mallard W. NIST chemistry WebBook, Nist standard reference database number 69. Gaithersburg: National Institute of Standards and Technology; 2011.

[69] Javadpour F. Nanopores and Apparent Permeability of Gas Flow in Mudrocks (Shales and Siltstone). PETSOC-09-08-16-DA 2009;48(08):16–21.

[70] Wang S, Feng Q, Javadpour F, Zha M, Cui R. Multiscale modeling of gas transport in shale matrix: an integrated study of molecular dynamics and rigid-pore-network model. SPE J 2020.